Rock Mechanics Bulletin 5 (2026) 100272

Contents lists available at ScienceDirect

Rock Mechanics Bulletin

journal homepage: www.keaipublishing.com/en/journals/rock-mechanics-bulletin

Thermo-mechanical coupling in cracked granite: Influence of crack inclination on fracture behavior and temperature evolution

Chenrui Huang[a,b,c], Chaomin Mu[b,c,*], Fei Wang[c], Yangyong Wu[d]

[a] *School of Mining Engineering, Anhui University of Science and Technology, Huainan, 232001, China*
[b] *School of Safety Science and Engineering, Anhui University of Science and Technology, Huainan, 232001, China*
[c] *State Key Laboratory of Digital and Intelligent Technology for Unmanned Coal Mining, Anhui University of Science and Technology, Huainan, 232001, China*
[d] *School of Mechanics and Photoelectric Physics, Anhui University of Science and Technology, Huainan, 232001, China*

ARTICLE INFO

Keywords:
Prefabricated crack
Infrared temperature measurement
Crack tip temperature
Thermo-mechanical coupling

ABSTRACT

Crack inclination angle (α) plays a critical role in the dynamic failure and thermo-mechanical coupling of granite, which is vital for rockburst monitoring and prevention. In this study, granite specimens with various prefabricated crack inclinations ($\alpha = 0^\circ, 30^\circ, 60^\circ, 90^\circ$) were tested using a split Hopkinson pressure bar (SHPB) system. Transient crack tip temperatures were monitored in real time by high-speed infrared thermography, and crack propagation was analyzed using digital image correlation (DIC). The results show that: 1) Propagation mode and mechanical properties: Increasing crack inclination causes a transition from pure tensile propagation to tension–shear mixed modes. At $\alpha = 60^\circ$, enhanced shear promotes branching cracks, while at $\alpha = 90^\circ$, crack closure suppresses propagation and induces localized damage. 2) Strength characteristics: Peak stress exhibits a "U-shaped" trend with respect to α, reaching the lowest value at $\alpha = 60^\circ$. 3) Thermal response: Crack tip temperature rise is strongly dependent on inclination. The maximum rise (up to 9.266 °C) occurs at $\alpha = 30^\circ$ and 60° due to pronounced tension-shear coupling and frictional slip, whereas $\alpha = 0^\circ$ and 90° show smaller increases. 4) Two-stage temperature evolution: Before peak stress, ~80% of the temperature rise originates from plastic work; after peak stress, crack slip and friction dominate, leading to accelerated heating. 5) Crack tip temperature rise serves as a sensitive indicator of local energy concentration and disaster risk, providing theoretical support for monitoring and prevention strategies in deep mining.

1. Introduction

Rocks are widely distributed in various underground engineering structures, and their dynamic properties and failure mechanisms play a crucial role in determining engineering stability. In deep mining (John et al., 2025; Wu et al., 2025), rockburst disaster prevention (Dou et al., 2014; Qiu et al., 2023; Dai et al., 2024), tunneling and underground storage construction, rocks are often subjected to high-strain-rate loading conditions, where crack propagation is the key mechanism governing rock instability. Rockburst is a violent dynamic failure of rock, typically occurring in deep, high-stress environments, characterized by the sudden fracturing and ejection of rock mass. Previous studies have demonstrated that crack propagation within the rock mass is the dominant failure mechanism and that the crack extension path and fracture mode ultimately determine the strength and stability of the rock (Hu et al., 2024). Particularly in deep, high-stress environments, crack extension is associated not only with stress concentration but also with thermo-mechanical coupling effects, leading to localized temperature increases at the crack tip (Wu et al., 2006). However, existing research on crack temperature evolution remains limited, especially regarding the effect of crack inclination on crack tip temperature evolution, which remains largely unexplored.

The fracture path and failure mode of cracks directly influence rock strength and stability, providing essential theoretical support for understanding rock fracture behavior under dynamic loading (Chen et al., 2012; Wang et al., 2022; Xiao et al., 2022; Li et al., 2023a; Peng et al., 2024a, 2024c; Yue et al., 2024). Wang et al. (2016a) investigated Mode I crack extension, revealing that crack propagation rates vary under loading, with possible stagnation (Ldhzsxl, 2017). Showing that increasing crack inclination shifts propagation from Mode I (tensile) to

---

* Corresponding author.
E-mail address: chmmu@mail.ustc.edu.cn (C. Mu).

Peer review under the responsibility of Chinese Society for Rock Mechanics & Engineering.

https://doi.org/10.1016/j.rockmb.2025.100272
Received 7 June 2025; Received in revised form 11 September 2025; Accepted 1 November 2025

Mode II (shear). Liu et al. (2023a) utilized SHPB tests and found that major cracks in granite specimens primarily manifest as wing cracks and coplanar cracks. Li et al. (2023b) investigated tensile-shear high-frequency emission waves induced by rock fracture, proposing a new method to identify crack propagation modes (Mode I and Mode II). Wu et al. (2021) explored crack front energy release rates and stress intensity factors (SIFs), introducing an enhanced VCCT method for non-smooth crack fronts. Liu et al. (2022) studied Mode I and Mode II stress intensity factors in CCBD specimens under distributed pressure and tangential friction, offering theoretical support for analyzing the effect of crack inclination on the stress field and temperature rise in the crack region.

Despite extensive research on crack propagation, studies on transient temperature changes in crack regions remain scarce. However, rockbursts pose a severe dynamic hazard in underground engineering, particularly in deep mining. During rockburst events, the crack region experiences a rapid temperature increase, as heat does not have sufficient time to diffuse into the surrounding environment. Therefore, an in-depth investigation into transient temperature evolution during rock rupture is critical for understanding crack extension mechanisms and energy dissipation processes, with significant implications for rockburst prediction, prevention, and control.

Currently, thermocouple-based rock temperature measurement is a well-established technique (Shao et al., 2018; Meng et al., 2024), but its slow response time makes it unsuitable for high-speed temperature monitoring. In contrast, infrared (IR) thermography offers rapid (Wang et al., 2023a; Kou et al., 2025) non-contact temperature measurement and has been widely applied in rock structure stability monitoring and non-destructive testing (NDT) of failure defects (Wu et al., 2001; Zhang et al., 2010; Mineo et al., 2019; Liu et al., 2023b; Peng et al., 2024b). Cao et al. (2023) examined the infrared radiation response of sandstone during loading and failure, establishing a temperature source density function for crack plastic zones. Wang et al. (2016b) used IRR evolution characteristics to predict rock damage and instability. Li et al. (2023c) applied high-speed infrared thermography (IRT) to analyze temperature evolution in water-bearing rocks and soils under impact loading, revealing that the formation of high-temperature shear cracks is closely related to crack inclination changes. Akdag et al. (2023) investigated crack propagation characteristics in granite under varying temperature conditions, uncovering the mechanism by which elevated temperatures accelerate granite fragmentation. Aihemaiti et al. (2025) analyzed rock failure modes, mechanical properties, and infrared radiation responses under different impact velocities, exploring the energy conversion mechanism and infrared temperature evolution in impact failure processes.

In transient temperature monitoring, the combination of HgTeGe infrared detectors and SHPB tests provides a foundation for temperature measurement during impact events (Xia et al., 1990; Mason et al., 1994; Potdar et al., 2004; Nieto-Fuentes et al., 2020). Liu et al. (2014) and Zhang et al. (2018) established temperature calibration curves for different materials through static experiments, enabling real-time surface temperature monitoring in combination with calibration curves, providing a reference for subsequent temperature measurement of non-homogeneous materials such as rocks. More recently, Huang et al. (2025) employed a self-developed high-speed infrared temperature measurement system combined with SHPB tests to investigate the thermo-mechanical coupling effects in rock and soil under impact loading. These studies have laid the foundation for dynamic temperature monitoring in transient rock failure, but further improvements in spatial and temporal resolution are needed to accurately characterize rock temperature evolution under extreme impact conditions and provide precise monitoring tools for rockburst prevention.

Although previous studies have explored crack propagation and temperature evolution in rocks under dynamic impact loading, most have primarily focused on the influence of impact loads on overall mechanical properties. However, research on how crack inclination angles affect localized temperature rise at the crack tip and the transient temperature variation during impact loading remains limited. Furthermore, as geological conditions and construction environments become increasingly complex, traditional rockburst prediction methods (Miao et al., 2016; Xue et al., 2021; Wang et al., 2024; Nan et al., 2025) often fail to meet the safety requirements of field applications.

To address these issues, this study utilizes a Split Hopkinson Pressure Bar (SHPB) apparatus to perform impact experiments on granite specimens with prefabricated cracks at varying inclination angles ($\alpha = 0^\circ$, 30°, 60°, 90°). High-speed infrared thermography is combined with digital image correlation (DIC) technology to enable real-time monitoring of both dynamic temperature evolution at the crack tip and the corresponding crack propagation morphology. This work systematically analyzes the effects of crack inclination on propagation mode, crack tip temperature development, and energy dissipation, with a particular focus on elucidating the coupled mechanisms between mechanical behavior and thermal response during the rock fracturing process. The results demonstrate that crack propagation, shear slip, and energy dissipation jointly influence temperature rise at the crack tip under dynamic loading. These findings offer critical thermodynamic parameters for monitoring rockburst precursors, thereby enhancing the accuracy and effectiveness of rockburst prediction and prevention in deep underground engineering.

2. Test equipment and program

2.1. Granite specimens

Granite specimens with dimensions of Φ 70 × 30 mm were prepared, with a 20 mm through-crack prefabricated at the center of the cylindrical surface to form a Center Straight Through Flattened Brazilian Disc (CSTFBD) specimens (Wang et al., 2015).

To precisely monitor the mechanical properties and temperature variations at the crack tip, the crack tips were sharpened, and the specimen surfaces were polished to ensure a maximum surface unevenness of 0.05 mm and a maximum non-parallelism of 0.02 mm between the upper and lower end faces. These refinements ensured close contact between the specimen and the loading rods, minimizing experimental errors. Additionally, to enhance the accuracy of digital image correlation (DIC) measurements, a uniform layer of white matte paint was sprayed on the specimen surface. After drying, a black marker pen was used to randomly apply ink speckles, forming a high-contrast pattern suitable for DIC analysis, as illustrated in Fig. 1.

2.2. High-speed infrared temperature measurement system principle and test design

2.2.1. Infrared temperature measurement principle

Infrared thermometry operates based on the Stefan-Boltzmann law, which establishes the relationship between an object's thermal radiation energy and its absolute temperature (Zhang et al., 2023). In practical applications, infrared sensors detect the thermal radiation emitted by the target object, and the temperature is determined using the following

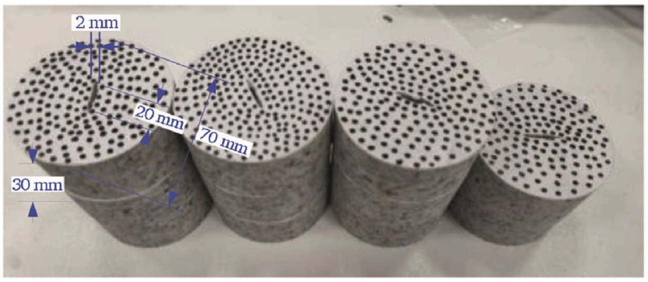

Fig. 1. Granite specimens.

Eq. (1),

$$T = \sqrt[4]{\frac{P(T)}{\gamma\eta}} \tag{1}$$

where T is the thermodynamic temperature of the target object, $P(T)$ denotes the total radiant energy radiated from the unit area of the target object per unit time when the temperature of the target object is T, which is called the total radiance, γ is the Stefan-Boltzmann constant, and η is the emissivity of the target object.

This theoretical framework underpins infrared thermometry, allowing for non-contact, real-time temperature monitoring in dynamic experiments.

2.2.2. Single-point high-speed infrared temperature measurement system test design

The single-point high-speed infrared temperature measurement system features a response frequency of up to 1 MHz, enabling microsecond-resolution temperature monitoring. The system comprises an optical assembly, a HgCdTe infrared detector, a preamplifier (MCT-1000), and a dynamic digital signal acquisition unit.

Under impact loading, transient surface temperature rises induce enhanced infrared emission, which is collected and focused by the optical system onto the detector and converted into an electrical signal. Owing to the low magnitude of the current output, the preamplifier is employed to strengthen the signal before it is digitized and recorded in real time. To minimize measurement error, the detector is cooled with liquid nitrogen (77 K), which effectively suppresses thermal noise and improves the signal-to-noise ratio, thereby ensuring reliable high-speed temperature acquisition.

The schematic configuration and calibration principle of the system are shown in Fig. 2. During calibration, a laser source emits a stable infrared beam, which is divided by a beam splitter into two paths: one for aligning the detector position using mirror reflection and the other for calibrating the specimen position.

Due to the varying emissivity of different materials, the temperature of the granite specimens was calibrated using an experimental approach (Guo et al., 2025; Huang et al., 2025). As shown in Fig. 3, the granite specimens were heated to different target temperatures for calibration. The surface temperature was measured simultaneously using a DELIXI DM-5005 infrared thermometer and the high-speed infrared measurement system to establish a calibration curve. The DM-5005 thermometer has a measurement range of −50 °C–900 °C, a resolution of 0.1 °C, a measurement accuracy of ±1.5 %, and an adjustable emissivity range of 0.10–1.00. For the granite specimens used in this study, the emissivity was set to 0.95 based on the infrared radiative characteristics of granite.

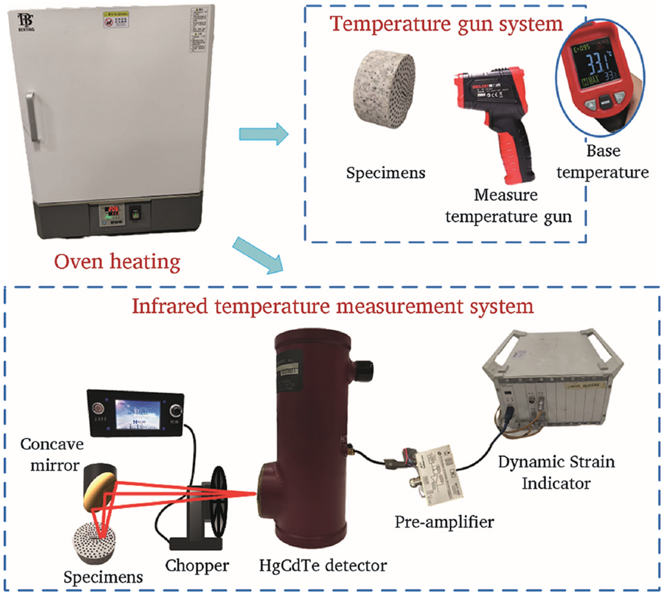

Fig. 3. Calibration flow chart.

In this experiment, the measured temperature variation is defined as ΔT, ranging from 0 to 100 °C. First, the temperature of the granite specimen was monitored multiple times at room temperature. The specimen was then placed in an oven for heating, and once the temperature stabilized, measurements were taken simultaneously using both the temperature gun and the high-speed infrared thermometry system. The temperature recorded by the temperature gun served as the reference temperature, while the voltage data from the infrared system was also collected. This calibration process was repeated multiple times to establish the relationship between temperature and voltage, generating a calibration curve as shown in Fig. 4.

The temperature-voltage fitting curve (Fig. 4) demonstrates a high fitting accuracy with a variance of $R^2 = 0.99$. The corresponding temperature-voltage fitting function is given as Eq. (2),

$$\triangle T = T - T_0 = -8.916\times10^{-5}\cdot U^2 + 0.194U + 0.372 \tag{2}$$

where ΔT is the amount of temperature change in °C, T is the real-time

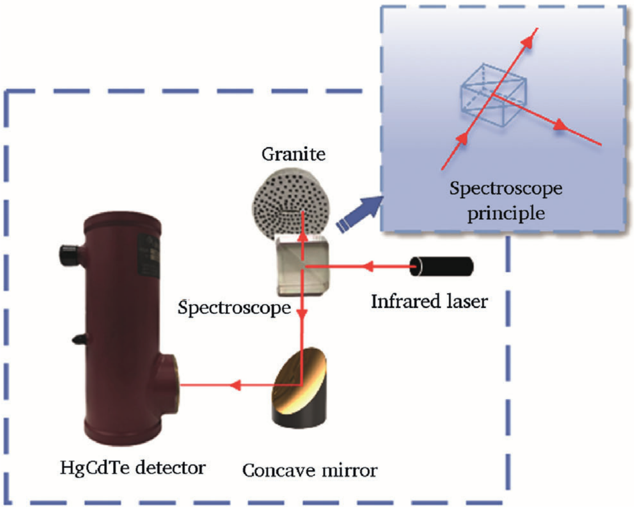

Fig. 2. Schematic diagram of high-speed infrared detector.

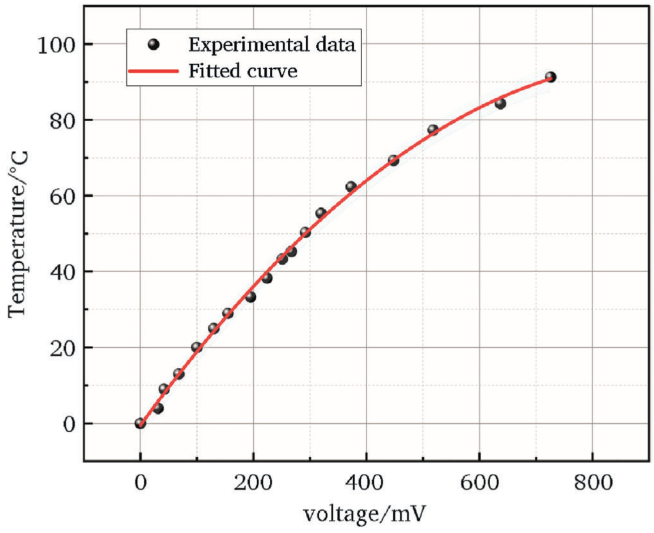

Fig. 4. Temperature-voltage fitting curve.

temperature in °C, T_0 is the room temperature in °C, U is the voltage in mV.

2.3. SHPB test setup

In this study, the Split Hopkinson Pressure Bar (SHPB) test system at the State Key Laboratory of Digital and Intelligent Technology for Unmanned Coal Minin was utilized. To meet the experimental requirements, a high-speed infrared temperature measurement system was integrated into the SHPB setup. The test system consists of a 400 mm-long striker bar, a 4000 mm-long incident bar, and a 2500 mm-long transmission bar, all with a diameter of 75 mm. The bars are made of high-strength 42CrMo alloy steel with a density of 7810 kg/m^3, an elastic modulus of 210 GPa, a wave velocity of 5190 m/s, and a Poisson's ratio of 0.23.

In the granite specimen splitting tests, strain gauge data were collected using a DHDAS dynamic signal acquisition system. During testing, the striker bar, propelled by high-pressure gas, impacts the incident bar axially, generating a compressive stress wave. The incident stress wave $\varepsilon_i(t)$ and the reflected stress wave $\varepsilon_r(t)$ are recorded on the incident bar, while the transmitted stress wave $\varepsilon_t(t)$ is recorded on the transmission bar. Based on one-dimensional stress wave theory and the assumption of stress uniformity, the Brazilian splitting test in conjunction with the two-wave method is used to derive the following Eq. (3),

$$\begin{cases} \sigma(t) = \dfrac{ED_0}{2DB}\varepsilon_{\mathrm{t}}(t) \\ \varepsilon(t) = -\dfrac{2c_0}{l_0}\displaystyle\int_0^t \varepsilon_r(t)dt \\ \dot{\varepsilon}(t) = -\dfrac{2c_0}{D}\varepsilon_r(t) \end{cases} \tag{3}$$

where $\varepsilon_{\mathrm{r}}(t)$ and $\varepsilon_{\mathrm{t}}(t)$ represent the reflected and transmitted stress waves at time t, respectively, D_0 and c_0 denote the diameter and wave velocity of the pressure bar, D and B represent the diameter and thickness of the granite specimens.

2.4. Test program and process

The impact rod was driven by high-pressure nitrogen, and its velocity was controlled by adjusting the gas pressure. To reduce transverse inertial oscillations, a loading shaper (0.3 mm thick, ~1.5 mm in diameter) was mounted on the impact ends of both the incident bar and the projectile. Given the short pulse duration (~160 μs for a 400 mm projectile), heat exchange with the environment was negligible, and the process was treated as adiabatic. The high-speed infrared temperature measurement system was aligned with the expected crack initiation zone on the front face of the specimen for precise monitoring, while the opposite surface was coated with a random speckle pattern for DIC. A high-speed camera was positioned to record crack evolution, as illustrated in Fig. 5.

When positioning the single-point high-speed infrared temperature measurement system, the heterogeneity of granite must be considered, as internal pre-stresses and external residual stresses may result in non-uniform temperature variations. To accurately monitor the temperature fluctuations at the crack, the region exhibiting the most pronounced temperature change is selected as the monitoring point. Since the crack tip experiences the highest stress concentration and most intense energy release, the primary focus of this experiment is on the temperature evolution at the crack tip of the granite specimen. The specific monitoring location is illustrated in Fig. 6.

When setting up the high-speed camera, a strong light source was utilized to ensure clear imaging of the scattering pattern on the granite surface. The camera was carefully adjusted to capture a sharp and well-defined scattering field, with a field of view of 150 mm × 100 mm, an image resolution of 0.38 mm/pixel, and an image acquisition frequency of 12,300 Hz. The entire process of crack initiation, propagation, and final failure of the granite specimen was recorded.

After each impact test, the recorded speckle images were processed using digital image correlation (DIC) software to extract the strain field, displacement field, and damage evolution. Simultaneous data acquisition was achieved using a DHDAS dynamic strain system, which recorded strain gauge signals from the incident bar, transmission bar, and infrared detector at 1 MHz. The DIC system was synchronized with the high-speed camera to enable real-time monitoring of specimen deformation.

In this study, four types of CSTFBD tests with varying crack inclination angles ($\alpha = 0°$, $30°$, $60°$, $90°$) were conducted to simulate crack propagation and transient temperature evolution at the crack tip under identical impact conditions. Preliminary tests revealed that when the impact air pressure was below 0.6 MPa, most of the energy was dissipated through crushing, leading to negligible temperature variation at the crack tip. Additionally, since deep mining, tunneling, and blasting engineering applications often subject rock masses to high-velocity impact loads, previous studies on low-velocity impacts (a few meters per second) have been insufficient to meet the demands of current engineering applications. Therefore, an impact air pressure of 0.8 MPa (corresponding to an impact velocity of approximately 24 m/s) was selected for testing granite specimens with different crack inclination angles ($\alpha = 0°$, $30°$, $60°$, $90°$).

3. Test results

3.1. Destruction process analysis

High-speed camera imaging was used to monitor granite specimens with varying crack inclination angles (α) in order to investigate the effects of crack inclination on the rock failure process and crack propagation paths. As shown in Fig. 7, the dynamic failure processes of granite specimens with different crack inclinations under impact loading are presented. To facilitate comparison of crack propagation paths, the images were processed in grayscale, with the main cracks in the original and grayscale images highlighted in green and yellow, respectively.

Under impact loading, the inclination angle α between the prefabricated crack and the loading direction critically controls the crack propagation mode and failure pattern. When $\alpha = 0°$, the crack is parallel to the loading direction and primarily subjected to tensile stress, resulting in rapid radial propagation and complete penetration through the specimen. As shown in Fig. 7a, a dominant main crack is clearly visible at 162.6 μs, leading to a clean bifurcation of the specimen along this crack. For $\alpha = 30°$, in addition to tensile stress, the crack plane is also subjected to a significant shear stress component. "Wing-shaped cracks" develop at the loading (incident) end and propagate toward both ends of the prefabricated crack, ultimately forming a "triangular wing-shaped crack" region, while a main crack emerges at the transmitted end. When $\alpha = 60°$, the crack propagation path becomes more complex due to greater shear stress on the crack plane. As shown in Fig. 7c, at 162.6 μs the crack path exhibits clear deflection and twisting, evolving into a mixed-mode propagation with prominent triangular wing-shaped extension zones. At $\alpha = 90°$, the prefabricated crack is perpendicular to the loading direction, inducing compressive stress normal to the crack plane and causing crack closure. In this case, an "axially symmetric triangular crack" region develops, accompanied by local shear slip. Owing to tensile stress at the transmitted end, an initial main crack forms in the middle of the prefabricated crack; by 162.6 μs, a complex network of cracks along the centerline and axially symmetric triangular extension regions are observed, eventually leading to specimen failure.

The DIC strain fields corroborate these observations: at $\alpha = 0°$, strain concentration localizes along a single crack path, whereas at $\alpha = 60°$ and $90°$, strain fields exhibit branching and rotation consistent with mixed-mode propagation. This confirms that α strongly influences the orientation of maximum tensile/shear stress and governs the complexity of

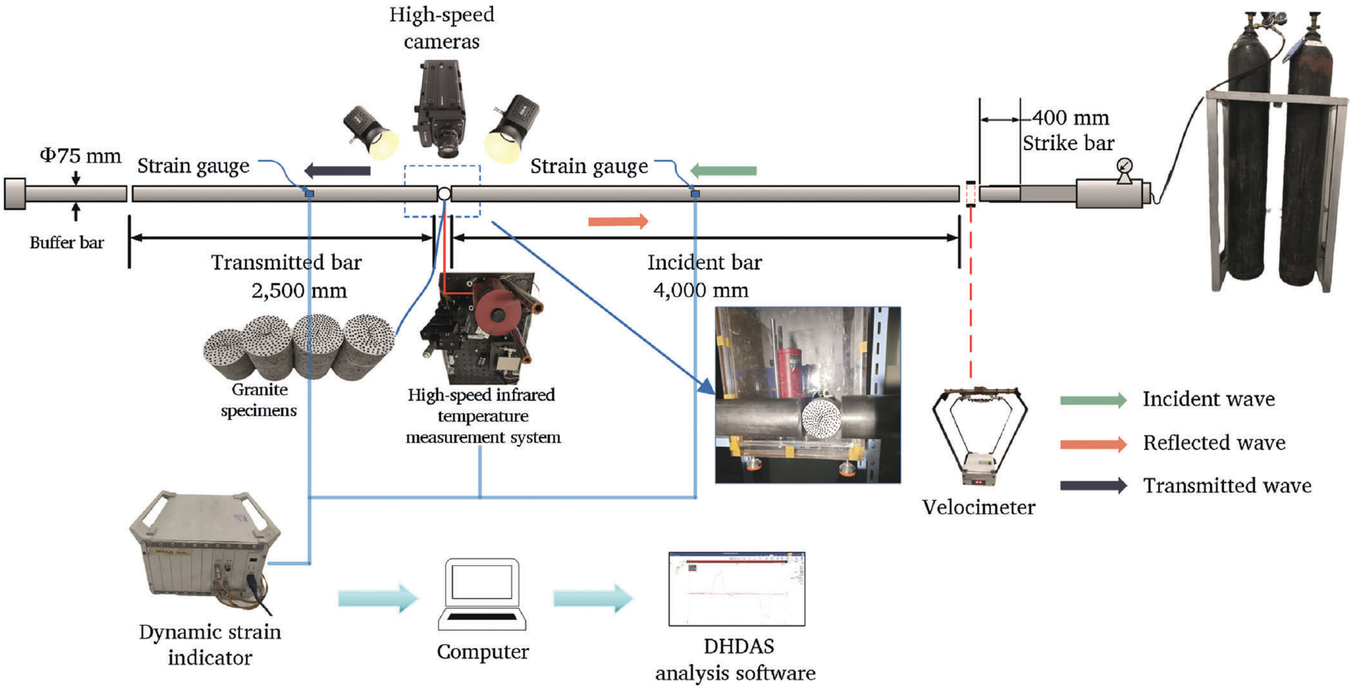

Fig. 5. SHPB test system based on high-speed infrared temperature measurement.

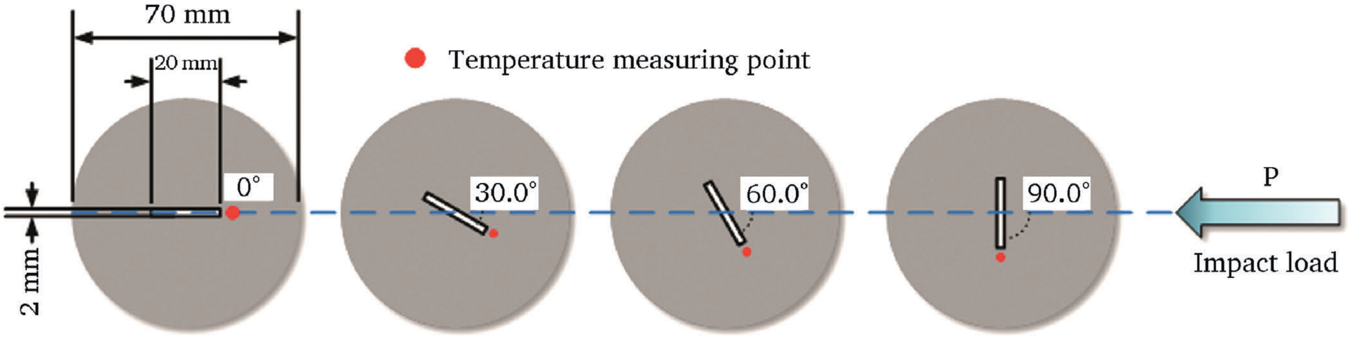

Fig. 6. Schematic diagram of temperature measurement points.

crack propagation. As α increases, the crack path transitions from a single, straight trajectory to multi-branched, triangular extension patterns at both incident and transmitted ends.

3.2. Dynamic property analysis

The tests were conducted at an air pressure of 0.8 MPa, corresponding to an impact velocity of approximately 24 m/s. To better illustrate the influence of cracks on the overall mechanical behavior of granite, a comparative analysis with intact rock samples was performed. However, as intact rock samples are not the primary focus of this study, they will not be further discussed in the subsequent analysis. Table 1 summarizes the test results. Due to a malfunction in the test velocimeter, impact velocities for two test groups were not recorded. However, all other test parameters remained normal, and the missing velocity data did not significantly affect the experimental results.

Due to the similar characteristics among multiple test groups, Group 1 was selected as the representative dataset for analysis. Fig. 8 presents the stress-time curves for both intact rock samples and granite specimens with different crack inclinations.

As shown in Fig. 8, the stress-time curves for intact rock samples and granite specimens with different crack inclination angles α exhibit a generally similar trend, but peak stress is significantly influenced by α.

When $\alpha = 0^\circ$, during loading, tensile stress directly acts on the crack. Since the crack is parallel to the loading direction, it remains closed, subjecting the crack surface to higher tensile stress. As a result, the specimen withstands greater stress, exhibiting the highest peak stress.

When $\alpha = 30^\circ$, the crack surface experiences both tensile and shear stresses, leading to a significant increase in stress concentration at the crack tip. The crack slips and propagates along its original direction, and due to the enhanced stress concentration effect, it becomes more prone to extension, resulting in a reduction in specimen strength.

When $\alpha = 60^\circ$, the crack surface is primarily subjected to shear stress, while tensile stress remains significant. This induces severe stress concentration at the crack tip, making the crack highly susceptible to propagation. Consequently, the load-bearing capacity of the specimen decreases, leading to the lowest peak stress.

When $\alpha = 90^\circ$, the crack is perpendicular to the loading direction, causing the crack surface to close, thereby reducing stress concentration and hindering crack propagation. As a result, the specimen sustains higher stresses, with peak stress comparable to that at $\alpha = 0^\circ$.

As shown in Fig. 9, the peak stress of intact rock samples was 56.37 MPa, while for specimens with crack inclination angles α of 0°, 30°, 60°, and 90°, the peak stresses were 39.17 MPa, 28.82 MPa, 24.73 MPa, and

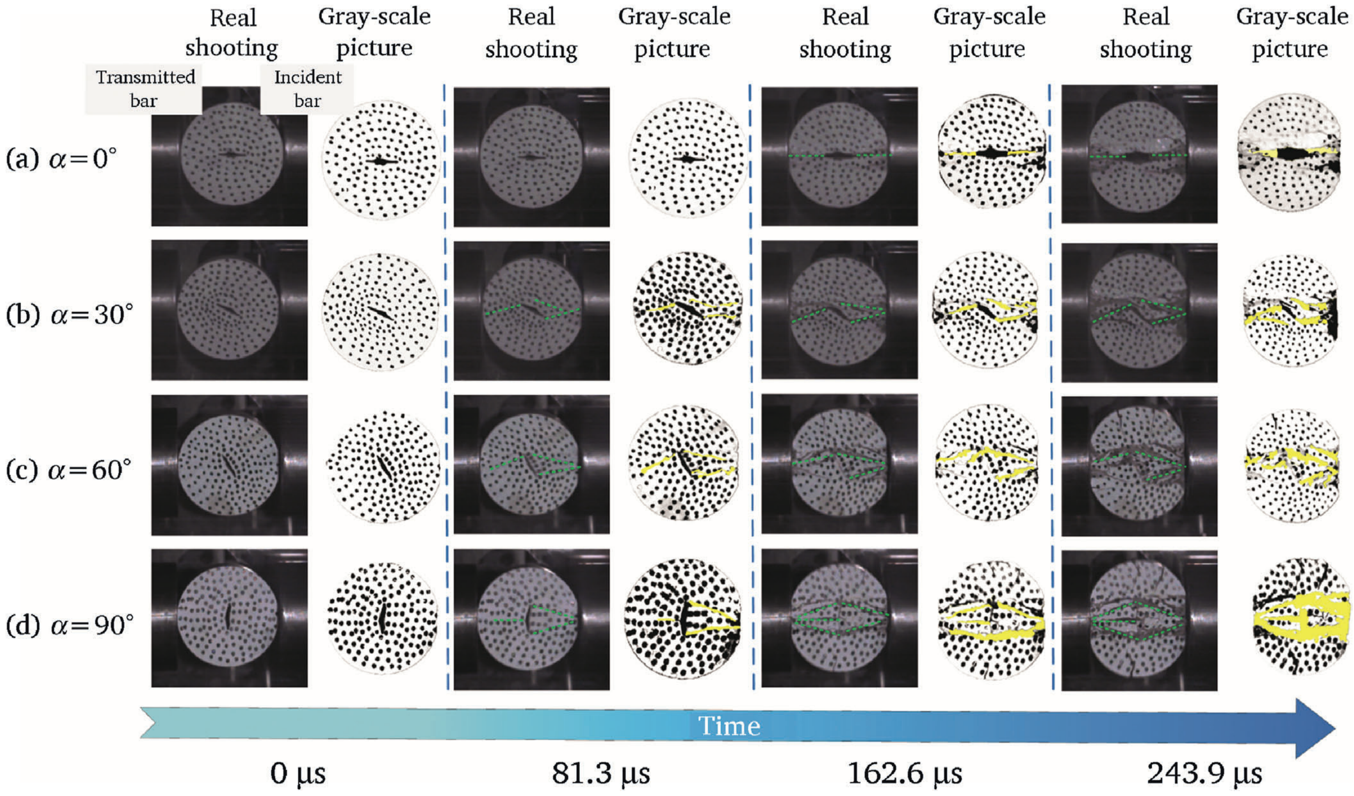

Fig. 7. Damage in the time course of impact with different inclination angle α splitting.

Table 1
Test result.

	α (°)	Impact velocity (m/s)	Impact strain rate (s^{-1})	Peak stress (MPa)
0	none	24.12	381.51	56.37
1-1-0	0	23.40	379.77	39.17
1-2-30	30	24.56	382.62	28.82
1-3-60	60	24.12	380.12	24.73
1-4-90	90	23.94	383.61	36.88
2-1-0	0	25.51	375.11	40.02
2-2-30	30	24.65	376.25	28.51
2-3-60	60	23.55	380.36	24.62
2-4-90	90	/	378.62	37.21
3-1-0	0	23.98	379.75	38.96
3-2-30	30	24.57	369.75	27.54
3-3-60	60	/	386.50	24.96
3-4-90	90	24.12	367.57	36.54

36.88 MPa, corresponding to reductions of 30.51%, 48.87%, 56.13%, and 34.58%, respectively. These results indicate that crack inclination has a significant effect on the tensile strength of granite. With increasing crack inclination angles α, peak stress initially decreases and then slightly recovers, forming a U-shaped trend. At $\alpha = 0°$ and $\alpha = 90°$, specimens exhibit higher peak stress, as cracks are less likely to propagate, leading to greater load-bearing capacity. At $\alpha = 30°$ and $\alpha = 60°$, peak stress significantly decreases, with $\alpha = 60°$ showing the lowest value. This is attributed to severe stress concentration and extensive crack propagation, resulting in the weakest load-bearing capacity.

3.3. DIC analysis

The Digital Image Correlation (DIC) method analyzes the evolution of strain and displacement fields by comparing images before and after rock deformation. In this study, an ultra-high-speed camera (12,300 Hz) was used to capture the granite failure process, and the strain and displacement field distributions were analyzed using DIC-2D software. To identify the most significant region of strain concentration, which corresponds to the most sensitive area for temperature variation, the radial strain and displacement fields of the specimens were selected for analysis, as shown in Fig. 10.

When $\alpha = 0°$, in the initial stage, strain is primarily concentrated at the crack, and as time progresses, the crack rapidly propagates in the radial direction. The strain field extends toward the crack tip, eventually leading to specimen splitting along the main crack direction. The strain distribution exhibits strong tensile stress concentration, particularly at the crack tip, indicating that crack propagation is predominantly controlled by tensile stress.

When $\alpha = 30°$, in the initial stage, strain is concentrated at the crack tip, and over time, the strain field reveals a significant shear stress effect, resulting in a complex crack propagation path. The strain concentration region expands toward both the crack tip and wing regions, demonstrating that crack propagation at $\alpha = 30°$ is influenced by both tensile and shear stresses, exhibiting a composite crack extension mode.

When $\alpha = 60°$, in the initial stage, strain concentration appears at both ends of the crack, and as time evolves, the strain field distribution becomes increasingly complex, with multi-directional strain concentration. This indicates that at $\alpha = 60°$, crack propagation is significantly influenced by shear stress, leading to highly complex crack paths, reflecting the non-uniform distribution of the stress field.

When $\alpha = 90°$, in the initial stage, strain is concentrated at the midsection of the crack, and as time progresses, the strain concentration region gradually expands to both sides of the crack. Eventually, the crack undergoes clear tensile fracture, forming a symmetrical strain distribution. The final fracture pattern aligns with the loading direction, confirming that at $\alpha = 90°$, crack extension remains strongly influenced by tensile stress.

The evolution of granite specimen damage over time can be effectively analyzed through the displacement field. When $\alpha = 0°$, the displacement is primarily concentrated on both sides of the crack, with

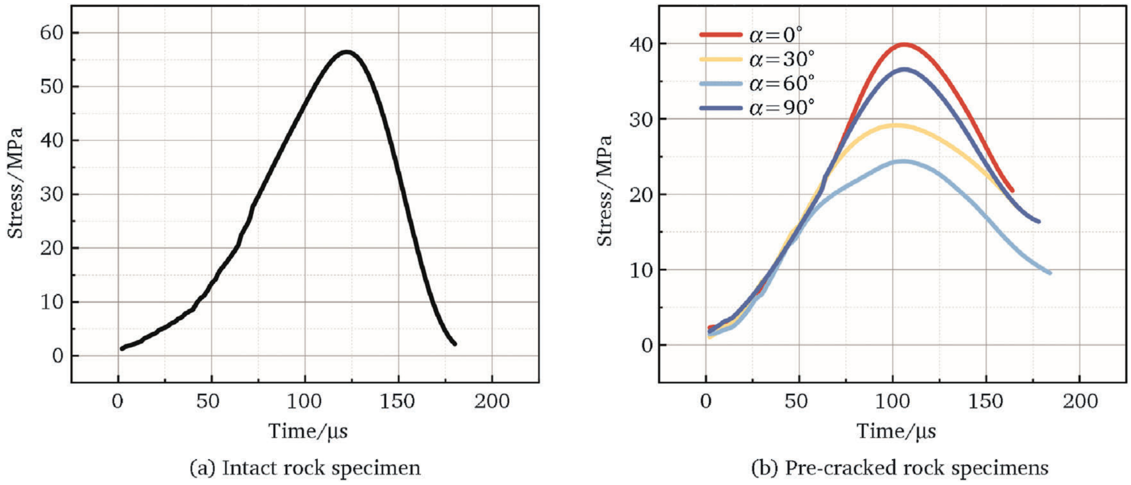

(a) Intact rock specimen (b) Pre-cracked rock specimens

Fig. 8. Granite stress-time history curve.

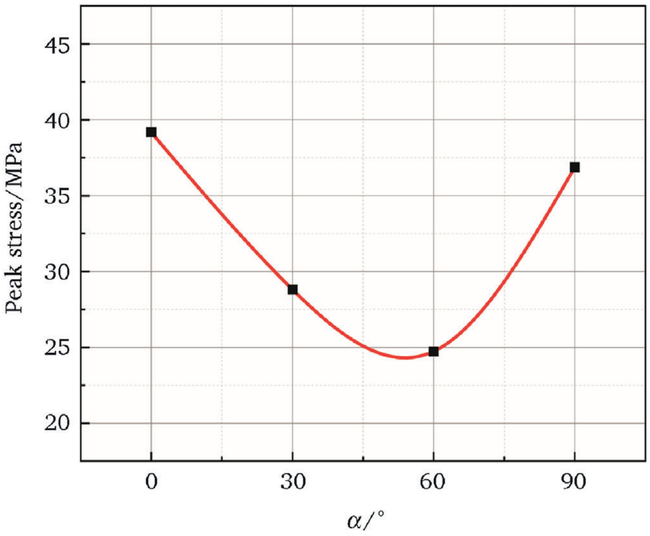

Fig. 9. Peak stress-α curve of granite.

rapid radial displacement increase near the crack tip. This leads to crack propagation along the radial direction, eventually penetrating the entire specimen. When $\alpha = 30^\circ$ and $\alpha = 60^\circ$, radial displacement is concentrated at the crack tip and the upper side of the crack, with pronounced shear displacement. As time progresses, the crack extends along both ends, exhibiting a certain inclination, leading to a more complex propagation path. When $\alpha = 90^\circ$, the crack is perpendicular to the loading direction, resulting in a more symmetric radial displacement field. This indicates that when a crack is perpendicular to the loading axis, it experiences a more uniform force distribution, causing significant material displacement on both sides.

With increasing crack inclination angles α, crack propagation complexity increases, and the strain and displacement field distribution evolves from simple radial extension to complex multi-directional crack propagation. This suggests that crack inclination not only influences crack propagation direction and path but also affects the displacement distribution of surrounding material. Furthermore, the crack tip is the most significant region of strain concentration and the most sensitive location for temperature variation, providing a crucial basis for temperature monitoring system design.

3.4. Dynamic temperature evolution

3.4.1. Thermal effects analysis

To enable more accurate and timely prediction of dynamic disasters such as rockburst, a high-speed infrared thermography system was established, and a series of SHPB tests were conducted to monitor the transient temperature evolution at the crack tip of granite specimens under impact loading in real time.

As illustrated in Fig. 11, which presents the Hopkinson bar signals and the corresponding crack tip temperature evolution, the temperature signal exhibits only a slight increase at the moment when the stress wave pulse reaches the specimen. However, a pronounced temperature rise occurs approximately 150 μs later. Although granite, as a high-density and low-porosity brittle material, possesses relatively high thermal conductivity, a certain degree of thermal lag is still observed. This phenomenon indicates that crack extension and interfacial friction induced by impact loading lead to gradual accumulation of local heat, resulting in a delayed temperature rise relative to the arrival of the stress wave.

Granite demonstrates a distinct thermo-mechanical coupling effect during impact-induced failure, further substantiating the crack tip frictional heating mechanism, wherein substantial energy concentration at the crack tip gives rise to significant thermal effects.

During impact testing, stress and temperature mutually influence each other, and the temporal evolution of stress and temperature for granite specimens with different crack inclination angles α exhibits generally similar trends. As shown in Fig. 12, to better analyze the relationship between stress-time and temperature-time curves at various inclination angles, the temperature corresponding to the stress peak ($\sigma_{\max}$) is defined as the peak stress temperature (ΔT_σ).

The stress and temperature-time curves in Fig. 12 demonstrate that the temperature evolution at the crack tip is closely related to the loading process. In the elastic stage, the granite primarily stores energy in the form of elastic strain energy, and the temperature remains nearly unchanged. Upon entering the plastic stage, stress becomes highly concentrated at the crack tip, and significant local plastic deformation and friction effects emerge. This concentration of stress, along with frictional heating, leads to a rapid temperature rise at the crack tip.

Due to stress concentration at the crack tip, plastic work is converted into heat, resulting in a temperature increase in this region. According to the first law of thermodynamics, the relationship for temperature rise due to plastic work can be expressed as Eq. (4),

$$\triangle T_p = \beta \frac{w/S}{\rho c_p} \tag{4}$$

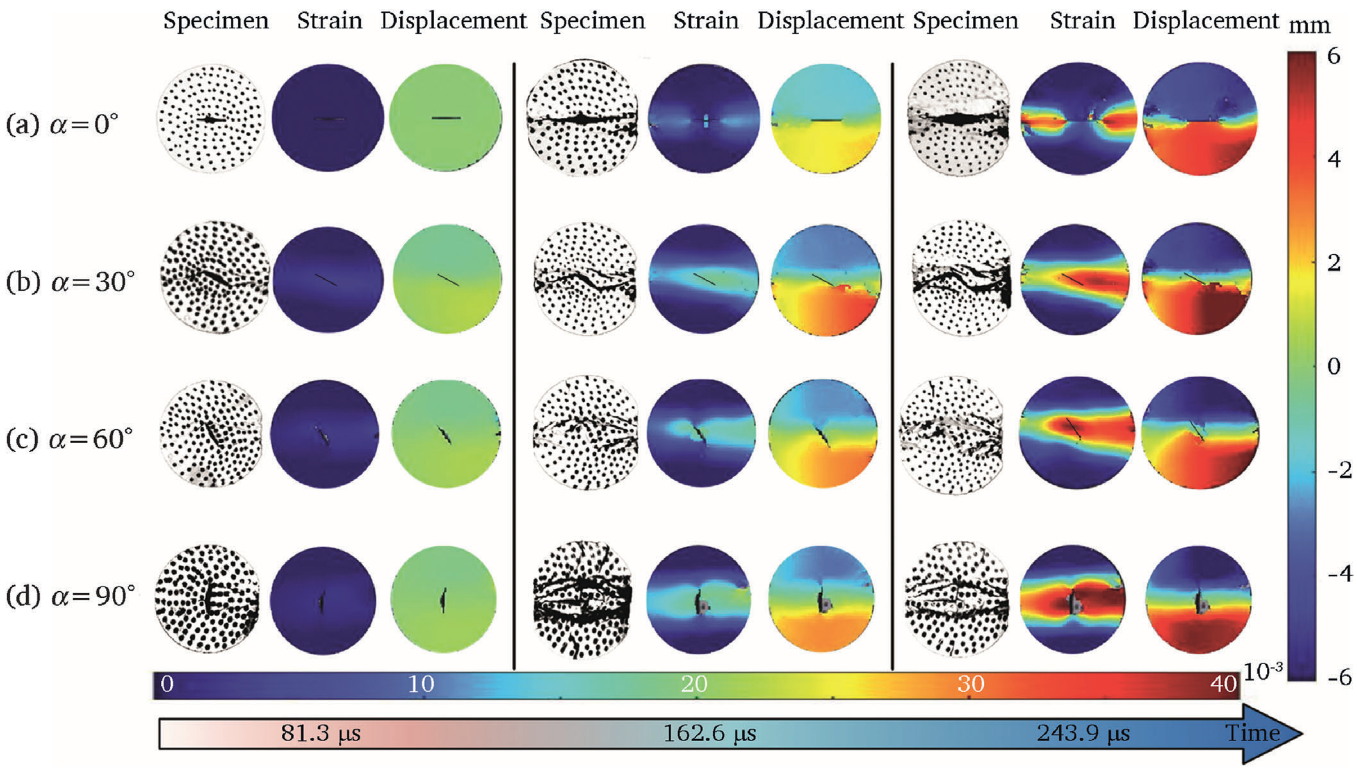

Fig. 10. Schematic diagram of DIC results for granite specimens.

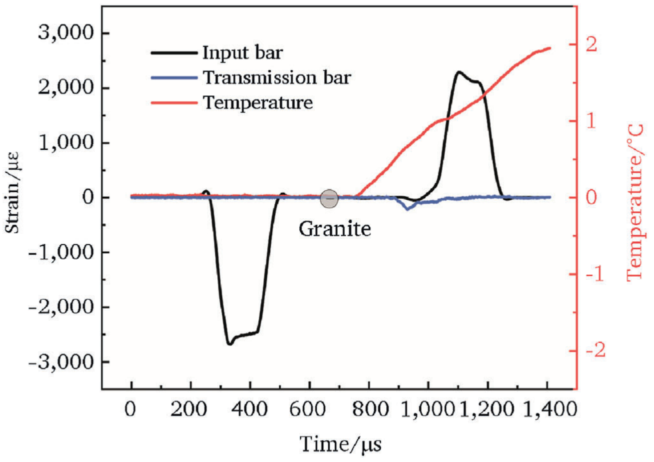

Fig. 11. Crack tip temperature of granite-SHPB waveform.

where ΔT_p is the temperature increase caused by plastic work, β is the plastic work conversion coefficient, w is the plastic work, c_p is the specific heat capacity at constant pressure for granite, ρ is the density of granite, and S is the area of temperature rise at the crack tip.

Meanwhile, the ratio n of the temperature rise due to plastic work (ΔT_p) to the peak stress temperature (ΔT_σ) is used to quantify the contribution of plastic work to the overall temperature increase, as shown in Table 2.

These results indicate that during the early stage of impact loading (0–100 μs), that is, prior to the peak stress, the temperature rise at the crack tip is mainly attributed to plastic work, with limited contribution from frictional heating. After the stress peak, the temperature at the crack tip continues to increase, which can be attributed to two factors: (1) the continued release of residual stress and micro-scale plastic deformation in the local crack tip region, and (2) the finite time required for heat conduction within the material, resulting in a sustained temperature rise. This temperature lag phenomenon demonstrates that the thermal response is delayed relative to the stress response, reflecting the non-synchronous nature of heat conduction and stress release.

The temperature evolution also varies with different crack inclination angles α:

When $\alpha = 0°$, the crack is parallel to the loading direction and subjected predominantly to tensile stress, leading to the highest stress concentration at the crack tip. This region of high stress rapidly generates local plastic deformation and friction, releasing a significant amount of heat. The thermo-mechanical coupling effect is strongest in this case, and substantial mechanical energy is converted into heat, causing a pronounced temperature rise.

When $\alpha = 30°$, the crack is influenced by both shear and tensile stress, resulting in a complex crack propagation path and significant local plastic deformation and friction at the crack tip. The temperature rise and its rate remain high, second only to $\alpha = 0°$, indicating that the conversion of mechanical to thermal energy is still considerable, although the strength of the thermo-mechanical coupling is somewhat reduced due to changes in the stress distribution.

When $\alpha = 60°$, the crack plane is dominated mainly by shear stress, with a relatively weaker tensile component. Frictional heating during crack propagation is less significant, and energy release at the crack tip is more closely related to plastic slip and relative displacement along the crack plane, leading to lower heat generation efficiency.

When $\alpha = 90°$, the crack plane is primarily under compressive stress, and crack propagation is inhibited, resulting in crack closure. Crack opening and slip at the tip are reduced, and the temperature rise is mainly due to plastic work, with minimal frictional heating. The mechanical energy at the crack tip is mainly used to overcome compressive stress, resulting in very limited heat generation.

A stronger thermo-mechanical coupling effect results in a more pronounced temperature rise at the crack tip. As the crack inclination angle α increases, the magnitude of temperature elevation at the crack tip gradually decreases, indicating that stress concentration is the dominant factor governing temperature evolution during crack

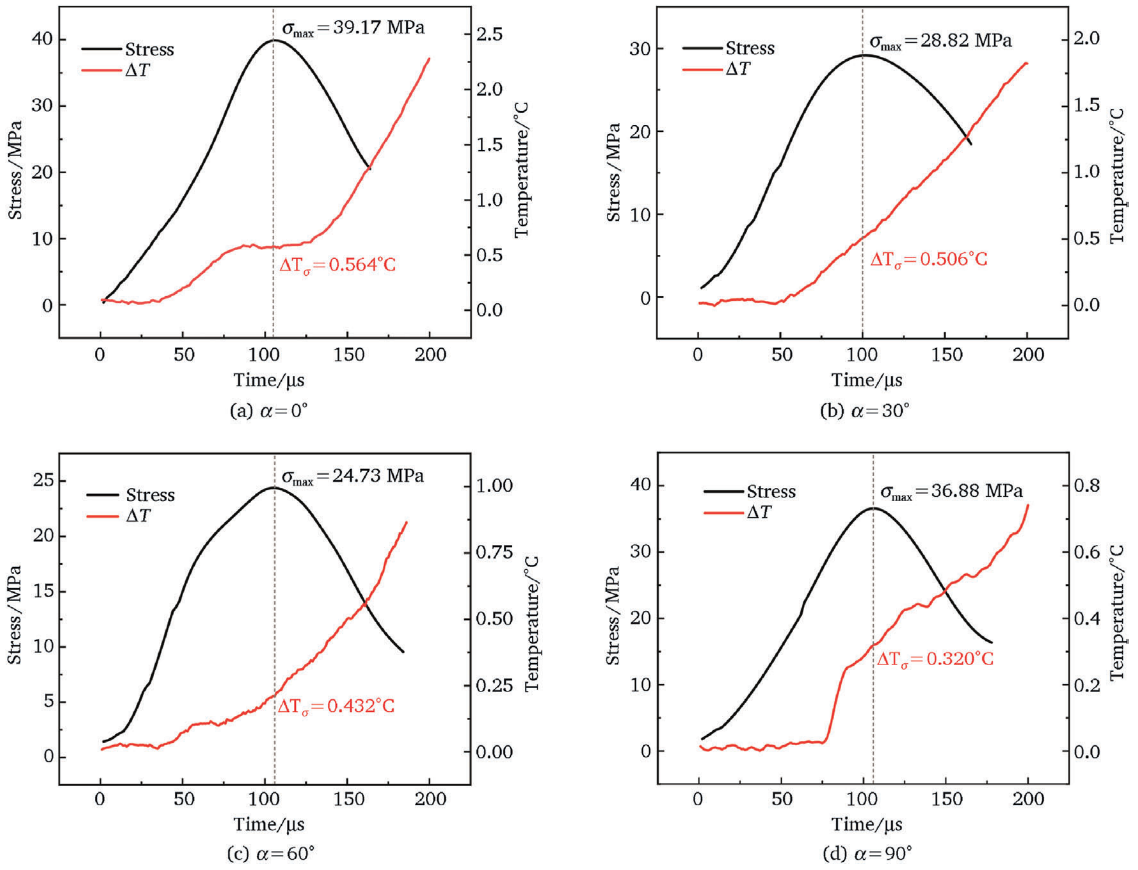

(a) $\alpha = 0°$ (b) $\alpha = 30°$

(c) $\alpha = 60°$ (d) $\alpha = 90°$

Fig. 12. Temperature-time history of α stress with different inclination angle.

Table 2
Ratio of plastic work contribution to crack tip temperature rise under different crack inclinations.

α/°	ΔT_p/°C	ΔT_σ/°C	n/%
0	0.446	0.564	79.1%
30	0.391	0.506	77.3%
60	0.365	0.432	84.5%
90	0.296	0.320	92.5%

propagation. The reduction in stress concentration with increasing α weakens the thermo-mechanical coupling effect accordingly. This coupling phenomenon captures the essential features of damage evolution in granite under dynamic impact conditions and offers important insights for advancing the understanding of rock fracture mechanisms.

3.4.2. *Temperature transient analysis*

During impact failure of granite containing cracks, the temperature evolution at the crack tip is governed by crack propagation, frictional heating, and stress wave transmission under dynamic loading. Notably, after reaching the peak stress, the granite is not completely fractured; localized friction and plastic deformation persist at the crack tip, generating substantial heat. To further elucidate the temperature evolution of cracks in granite under impact, the entire process (approximately 800 μs) was analyzed.

As shown in Fig. 13, the temperature evolution curves of crack tips with different inclination angles α follow a similar pattern: a slow initial rise, a rapid increase, a peak, and a subsequent decline. Before the peak stress (approximately 0–100 μs), the specimen maintains its global load-bearing capacity, and stress is concentrated near the crack tip. In this stage, microplastic deformation within the crack-tip process zone is the primary heat source, contributing about 80% of the total temperature rise.

After the peak stress, the specimen's macroscopic strength drops sharply, but the crack faces remain partially in contact. Pronounced interfacial sliding occurs, generating significant frictional heat. This is evidenced by the continued-and often accelerated-temperature rise even as the stress rapidly decays, indicating that frictional dissipation, rather than plastic work, dominates the post-peak thermal response.

This transition from a plastic-work-dominated pre-peak stage to a friction-dominated post-peak stage reveals the shift in energy dissipation mechanisms during dynamic rock fracture and highlights the importance of crack-interface slip in governing late-stage temperature evolution.

Although the overall trend of temperature rise is similar for different crack inclinations α, the peak temperatures are strongly dependent on α. For $\alpha = 0°$, the crack is parallel to the loading direction, resulting in high stress concentration and a higher temperature rise within the first 100 μs; however, because tensile stress dominates and friction is relatively limited, the peak temperature is moderate (6.026 °C). For $\alpha = 30°$, a combination of tensile and shear stresses leads to a complex stress state at the crack tip, with both friction and plastic deformation strongly pronounced, yielding the highest peak temperature (9.266 °C). For $\alpha = 60°$, shear stress dominates crack propagation, and frictional heating is prominent, resulting in a slightly lower peak temperature compared to $\alpha = 30°$. When $\alpha = 90°$, the crack surfaces close and propagation is suppressed; frictional heating is minimal, and the peak temperature is the lowest, indicating the weakest thermo-mechanical effect. These results reveal that crack tip temperature rise provides insight into local energy dissipation and the variation of thermo-mechanical effects with crack inclination.

To further investigate the influence of crack inclination angle α on crack tip temperature rise, the peak temperatures corresponding to different inclination angles were compared, as shown in Fig. 14.

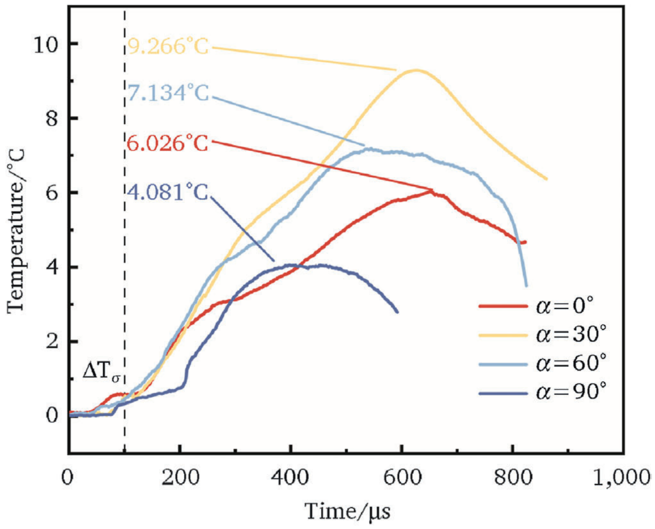

Fig. 13. Crack tip temperature-time curve.

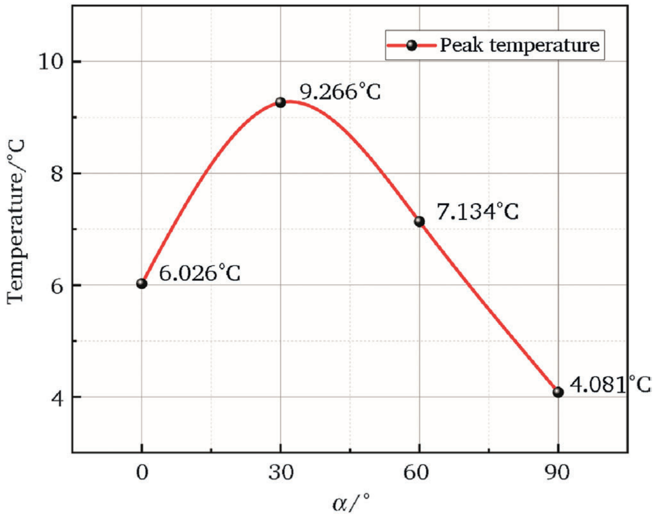

Fig. 14. Temperature-dip angle α curve of granite.

The results reveal a significant relationship between crack inclination and temperature rise, with the peak temperature exhibiting a clear "increase-then-decrease" trend as α varies. As α increases from 0° to 30°, the peak temperature rises sharply, reaching a maximum value of 9.266 °C. With further increases in α to 60° and 90°, the peak temperature gradually declines to 7.134 °C and 4.081 °C, respectively. This pattern indicates that, at a crack inclination of 30°, local energy dissipation and frictional heating at the crack tip are most intense, resulting in the highest temperature rise. As the inclination angle further increases, the local stress state at the crack tip shifts from tensile–shear coupling to primarily shear or closed modes, causing a reduction in both energy dissipation and thermo-mechanical effects. Overall, the non-monotonic relationship between peak temperature and crack inclination reflects the strong coupling between localized stress states and heat dissipation mechanisms at the crack tip.

These findings highlight the significant impact of crack inclination on the thermal effects during dynamic failure of granite. Notably, regions with crack inclination angles between 30° and 60° may become high-temperature anomaly zones and energy concentration points during rockburst nucleation, thus increasing the risk of rockburst occurrence.

4. Discussion

Rockburst is a sudden and violent rock dynamic disaster that frequently occurs in deep mining, tunnel excavation, high and steep slopes, and underground caverns (Sun et al., 2024; Luo et al., 2025). Its occurrence mechanism is closely related to the in-situ stress state, crack propagation dynamics, and thermo–mechanical coupling conditions of the surrounding rock. Previous studies have shown that temperature not only affects the mechanical properties of rock but may also intensify the tendency for rockburst (Chen et al., 2014; Lu et al., 2025). At present, the prediction and monitoring of rockburst rely heavily on techniques such as acoustic emission (AE), microseismic monitoring, and stress field reconstruction (Wu et al., 2021; Wang et al., 2023; Yang et al., 2024; Zhang et al., 2024a; Zhao et al., 2024; Li et al., 2025). In recent years, several scholars have attempted to incorporate thermal indicators into rockburst monitoring (Zhang et al., 2024b). For example, Zhang et al. (2024c) combined infrared radiation energy with acoustic emission energy to establish a quantitative rockburst damage evaluation model. However, most of these studies focus on low-strain-rate, quasi-static conditions and fail to accurately capture the transient crack-tip temperature evolution under high strain-rate and strong dynamic disturbances.

To address this limitation, this study employed a high-speed infrared temperature measurement system combined with SHPB dynamic loading to systematically simulate and record the effect of different crack inclination angles (α) on the dynamic crack-tip temperature evolution of granite under rockburst-like conditions. The results revealed a distinct two-stage temperature evolution pattern: in the pre-peak stage (approximately 0–100 μs), plastic work dominates and accounts for about 80% of the total temperature rise. The temperature rise is highly sensitive to local stress concentration and thus has potential early-warning significance. In particular, when $\alpha = 0°$, the crack is parallel to the loading direction, resulting in pronounced stress concentration and the highest early-stage temperature rise (0.564 °C within 100 μs), indicating substantial energy accumulation at the crack tip. After the peak stress, crack propagation and interface sliding become intense, frictional heating becomes the dominant mechanism, and the temperature rises rapidly. In the specimens with $\alpha = 30°$ and 60°, tension-shear coupling and sliding are most pronounced, leading to the highest rate and magnitude of temperature rise (with a maximum of 9.266 °C at $\alpha = 30°$). In contrast, when $\alpha = 90°$, the crack faces are closed, crack propagation is restricted, and the temperature rise is minimal.

These results indicate that the local crack-tip temperature rise is jointly controlled by the combined effects of crack inclination and stress state, exhibiting a transition in energy dissipation mechanism from plastic-work dominance to frictional-work dominance. He et al. (2025) defined rockburst as “a sudden failure of rock mass surrounding the excavations caused by the rapid release of stored energy when induced stresses exceed the rock strength.” Furthermore, comparison of the present findings with studies on energy conversion suggests that the pre-peak temperature rise corresponds to the stage of energy accumulation and charge build-up, whereas the post-peak temperature rise reflects rapid energy release and discharge-like phenomena. This observation is highly consistent with the electric spark phenomena reported by Li et al. (2021) and Lu et al. (2021) during roof rock fracture. Therefore, crack-tip temperature rise is not only a thermal response parameter but also a key indicator for thermo-acoustic-electromagnetic joint monitoring. Coupling temperature measurements with acoustic emission, microseismic, and electromagnetic signals is expected to enable earlier detection and more accurate prediction of rockbursts in deep mining.

5. Conclusion

(1) The crack inclination angle α has a significant influence on both the mechanical properties and crack propagation path of granite.

As α increases, the crack propagation mode evolves from pure tensile to a mixed-mode dominated by tensile-shear, with enhanced shear stress leading to an increased number of crack branches. The peak strength of specimens with cracks is reduced by up to 56.13% compared to intact granite. When $\alpha = 90^\circ$, the crack surfaces are closed, crack propagation is restricted, and an axially symmetric and complex failure pattern is observed, resulting in higher residual strength. The variation of peak stress with α follows a “U-shaped” trend, reaching its minimum at $\alpha = 60^\circ$, where the shear effect is most pronounced.

(2) The crack tip consistently acts as the main region of strain and displacement concentration, serving as the dominant zone for crack propagation and energy dissipation. For small inclination angles, strain concentration and crack propagation are primarily radial; as α increases, multiple shear bands develop, resulting in significantly more complex crack paths. The increase in crack inclination not only raises the spatial complexity of strain and displacement field distributions but also affects the local mechanical and thermal responses at the crack tip. DIC analysis confirms that the crack tip is also the most sensitive region for temperature changes, providing both theoretical and experimental support for monitoring crack tip thermal effects and predicting crack extension.

(3) The temperature rise at the crack tip is strongly correlated with the crack inclination angle α. For $\alpha = 0^\circ$, the crack tip is mainly controlled by tensile stress, with pronounced stress concentration and relatively weak frictional effects, resulting in a peak temperature of 6.026 °C. As α increases, the stress state at the crack tip becomes more complex; under tensile–shear coupling, frictional and plastic deformation effects are enhanced, leading to a significant increase in temperature, with the peak reaching 9.266 °C at $\alpha = 30^\circ$. When $\alpha = 90^\circ$, the crack surfaces tend to close, and the temperature rise at the crack tip is minimized. Overall, the temperature rise at the crack tip reflects local differences in energy dissipation and thermo-mechanical effects under different inclination angles, providing important physical insights into the dynamic response of rock governed by crack propagation.

(4) The temperature evolution at the crack tip reflects the stage-dependent nature of the energy dissipation mechanism. Before the stress peak, the temperature rise is mainly attributed to local plastic work, accounting for approximately 80% of the total. After the stress peak, sliding and interfacial friction at the crack surfaces become significant, making frictional heating the dominant contributor to the continued temperature rise. For $\alpha = 30^\circ$–60°, higher temperature rises are observed, indicating the potential for local energy concentration and disaster risk under tensile–-shear coupled conditions. The thermo-mechanical coupling effects at the crack tip are of critical importance for the nucleation, energy accumulation, and monitoring of dynamic disasters, and hold substantial engineering value for the thermal field perception and mitigation of deep rock mass hazards.

CRediT authorship contribution statement

Chenrui Huang: Writing – original draft, Validation, Formal analysis, Data curation. **Chaomin Mu:** Writing – review & editing, Project administration, Funding acquisition. **Fei Wang:** Validation, Supervision. **Yangyong Wu:** Writing – review & editing, Visualization.

Declaration of competing interest

All authors have read and approved the final manuscript and confirm that there is no conflict of interest regarding the publication of this research.

Acknowledgements

The authors gratefully acknowledge the financial support from National Key Research and Development Program of China (No. 2021YFC3100802), Anhui Engineering Research Center of New Explosive Materials and Blasting Technology (No. AHBP2023B-09).

References

Aihemaiti, A., Li, Z.H., Yin, S., Wang, X.R., Hu, Q.J., Zang, Z.S., Tian, H., Zhang, X., 2025. Study on the impact damage behavior and infrared radiation evolution characteristics of rock under different drop hammer velocities. Infrared Phys. Technol. 145 (2025), 105648.

Akdag, S., Karakus, M., Nguyen, G.D., Taheri, A., Zhang, Q.-B., Zhao, J., 2023. Dynamic response and fracture characteristics of thermally-treated granite under dynamic loading. Int. J. Rock Mech. Min. Sci. 170, 105482.

Cao, K.W., Dong, F.R., Yu, Y.H., Khan, N.M., Hussain, S., Alarifi, S.S., 2023. Infrared radiation response mechanism of sandstone during loading and fracture process. Theor. Appl. Fract. Mech. 126 (2023), 103974.

Chen, X., Liao, Z.H., Peng, X., 2012. Deformability characteristics of jointed rock masses under uniaxial compression. Int. J. Min. Sci. Technol. 22 (2), 213–221.

Chen, G., Li, T., Zhang, G., Yin, H., Zhang, H., 2014. Temperature effect of rock burst for hard rock in deep-buried tunnel. Nat. Hazards 72 (2), 915–926.

Dai, J., Gong, F., He, Z., Xu, L., 2024. Quantitative estimation of potential rockburst pit depths during blasting excavation in deep tunnels. Int. J. Rock Mech. Min. Sci. 178, 105748.

Dou, L.M., Mu, Z.L., Li, Z.L., Cao, A.Y., Gong, S.Y., 2014. Research progress of monitoring, forecasting, and prevention of rockburst in underground coal mining in China. Int J Coal Sci Technol 1 (3), 278–288.

Guo, L.G., Liu, A.K., Huang, C.R., Mu, C.M., 2025. High-speed IR temperature measurement system. Infrared Technol. 47 (1), 36–43.

He, M., Canbulat, I., Suorineni, F.T., Karakus, M., Nie, W., Liu, D., Zhang, C., Nagibin, A., Rustembek, B., 2025. Definition and classification of rockburst. Rock Mech Bull 4 (3), 100206.

Hu, M., Tan, Q.T., Feng, D.L., Ren, Y., Huang, Y., 2024. Simulation of rock crack propagation and failure behavior based on a mixed failure model with SPH. Rock Mech. Rock Eng. 57 (11), 9575–9596.

Huang, C., Mu, C., Liu, A., Huang, X., Zhang, C., 2025. Study on dynamic properties and dynamic temperature of concrete under high-speed impact. Explos. Shock Waves. 45 (5), 053101-053101.

John, W., Canbulat, I., Zhang, C., Wei, C., 2025. Energies within rock mass and the associated dynamic rock failures. Rock Mech. Rock Eng. 1–24.

Kou, G.J., Yang, Z.W., He, K.C., Zhang, W., Zhang, S.S., Liu, M.Q., Zhang, Y., 2025. Evaluation for tensile failure process of NOL rings based on infrared thermography. Infrared Phys. Technol. 144, 105628.

Ldhzsxl, Xibing, 2017. Characteristics of dynamic failure of marble with artificial flaws under split hopkinson pressure bar tests. Chin. J. Rock Mech. Eng. 36 (12), 2872–2883.

Li, M., Lu, Y., Shi, S., Li, H., Tian, Z., Ye, Q., Lu, J., 2021. Piezoelectric effect and ignition properties of coal mine roof sandstone deformation and fracture. Fuel 290, 120007.

Li, P., Su, G., Xu, H., He, B., 2023a. Quantitative detection of damage processes in granite by sound signals. Int. J. Rock Mech. Min. Sci. 164, 105356.

Li, H., Wang, F., Chen, F., Deng, J., Zhao, S., 2023b. Comparison of high-frequency components in acoustic emissions from rock fracture under mode I and Mode II dominated loading. Int. J. Rock Mech. Min. Sci. 170, 105554.

Li, X.L., Li, Z.H., Yin, S., Lei, Y.Y., Niu, Y., Tian, H., Song, X.Y., Zhang, X., Zang, Z.S., Lou, Q., 2023c. Experimental study on infrared thermal response characteristics of water-bearing concrete under drop hammer impact. Infrared Phys. Technol. 135 (2023), 104899.

Li, J., Guo, S., Yang, G., Qi, S., 2025. The influence of faults on adjacent rock mechanical behavior and acoustic emission characteristics: a case study of the xianshuihe fault zone. Rock Mech Bull, 100210.

Liu, Y.G., Tang, Z.P., Cui, S.T., 2014. Real-time measuring methods for transient temperature under shock loading. Explos. Shock Waves 34 (4), 471–475.

Liu, J., Li, Y., Qiao, L., 2022. Analytical solutions of stress intensity factors for a centrally cracked Brazilian disc considering tangential friction effects. Rock Mech. Rock Eng. 55 (4), 2459–2470.

Liu, T., Ding, L., Wang, G., Ma, R., Li, X., 2023a. Dynamic properties and failure mechanism of granite with non-persistent joints subjected to impact load. Int. J. Rock Mech. Min. Sci. 169, 105451.

Liu, W., Ma, L.Q., Gao, Q.Q., Spearing, A.J.S., Wang, Y.Y., Cui, R.Y., Zhao, Z.Y., 2023b. Fracture precursor recognition and damage quantitative characterization of stressed rock using infrared radiation. Rock Mech. Rock Eng. 56 (8), 5567–5584.

Lu, Y., Li, M., Wang, D., Shi, X., Li, H., Zhu, Y., Ye, Q., Lu, J., 2021. Discharge and ignition characteristics from indentation fracture of coal mine roof. Fuel 291, 120208.

Lu, H., Qi, Y., Chen, W., Li, C., Li, X., 2025. Coupling effect of temperature and confining pressure on fracture toughness of transversely isotropic shale: insights from a thermal-mechanical DEM model. Rock Mech Bull., 100211

Luo, S., Yuan, Q., Zhihong, D., Liming, Z., Chunhua, Z., Zhaowei, Y., Peng, Y., 2025. Control of rock burst during deep tunnel blasting excavation based on energy release process optimizing. Rock Mech Bull. 5 (1), 100239.

Mason, J.J., Rosakis, A.J., Ravichandran, G., 1994. On the strain and strain rate dependence of the fraction of plastic work converted to heat: an experimental study using high speed infrared detectors and the kolsky bar. Mech. Mater. 17 (2), 135–145.

Meng, F.Z., Han, J.H., Li, Z.Y., Wang, F.L., Yue, Z.F., Cai, Q.J., Cui, G.H., Zhou, H., 2024. The sequence of heating and loading affects shear properties of granite fractures under high temperature. Rock Mech. Rock Eng. 57 (9), 6543–6566.

Miao, S.-J., Cai, M.-F., Guo, Q.-F., Huang, Z.-J., 2016. Rock burst prediction based on in-situ stress and energy accumulation theory. Int. J. Rock Mech. Min. Sci. 83 (86–94).

Mineo, S., Pappalardo, G., 2019. InfraRed thermography presented as an innovative and non-destructive solution to quantify rock porosity in laboratory. Int. J. Rock Mech. Min. Sci. 115, 99–110.

Nan, T., Dou, L., Małkowski, P., Cai, W., Li, H., Liu, S., 2025. Applicability of existing criteria of rockburst tendency of sandstone in coal mines. Int. J. Min. Sci. 35 (3), 417–431.

Nieto-Fuentes, J.C., Osovski, S., Rittel, D., 2020. High-speed infrared thermal measurements of impacted metallic solids. MethodsX 7 (2020), 100914.

Peng, L., Yue, Z., Wang, X., Zhou, J., 2024c. Experimental study on the interaction mechanism of two dynamic cracks under blasting loading. Int. J. Rock Mech. Min. Sci. 184, 105956.

Peng, Z., Su, X., Chen, Y., Xia, J., Li, D., 2024a. Characteristic stress and strain precursor information for fine-grained granite during failure process under triaxial loading and unloading conditions. Rock Mech Bull 3 (1), 100101.

Peng, S.J., Yang, Y., Xu, Q.F., Xu, J., Qin, C.L., Nong, X.L., 2024b. Study on impact tendency and damage characteristics of rock-like materials based on Acoustic and thermal responses. Rock Mech. Rock Eng. 57 (12), 10367–10383.

Potdar, Y.K., Zehnder, A.T., 2004. Temperature and deformation measurements in transient metal cutting. Exp. Mech. 44 (1), 1–9.

Qiu, J., Xie, H., Zhu, J., Wang, J., Deng, J., 2023. Dynamic response and rockburst characteristics of underground cavern with unexposed joint. Int. J. Rock Mech. Min. Sci. 169, 105442.

Shao, W., Li, X., Sun, Y., Huang, H., Tang, J., 2018. An experimental study of temperature at the tip of point-attack pick during rock cutting process. Int. J. Rock Mech. Min. Sci. 107, 39–47.

Sun, J., Liu, D., He, P., Guo, L., Cao, B., Zhang, L., Li, Z., 2024. Experimental investigation on acoustic emission precursor of rockburst based on unsupervised machine learning method. Rock Mech Bull 3 (2), 100099.

Wang, Q.Z., Yang, J.R., Zhang, C.G., Zhou, Y., Li, L., Zhu, Z.M., Wu, L.Z., 2015. Sequential determination of dynamic initiation and propagation toughness of rock using an experimental–numerical–analytical method. Eng. Fract. Mech. 141, 78–94.

Wang, M., Zhu, Z.M., Wang, X., 2016a. The growth of mixed-mode I/II crack under impacting loads. Chin. J. Rock Mech. Eng. 35 (7), 1323–1332.

Wang, C., Lu, Z., Liu, L., Chuai, X., Lu, H., 2016b. Predicting points of the infrared precursor for limestone failure under uniaxial compression. Int. J. Rock Mech. Min. Sci. 88, 34–43.

Wang, G., Song, L.B., Liu, X.Q., Bao, C.Y., Lin, M.Q., Liu, G.J., 2022. Hear fracture mechanical properties and acoustic emission characteristics of discontinuous jointed granite. Rock Soil Mech. 43 (6), 1533–1545.

Wang, F., Sheng, J., Sfarra, S., Zhou, Y.H., Xu, L.X., Liu, L.X., Chen, M.J., Yue, H.H., Liu, J.Y., 2023a. Multimode infrared thermal-wave imaging in non-destructive testing and evaluation (NDT&E): physical principles, modulated waveform, and excitation heat source. Infrared Phys. Technol. 135, 104993.

Wang, Y., Tang, Ca, Cai, M., Tang, L., Ma, T., Zhang, S., Li, L., Li, Y., 2023b. Microseismicity evolution related to two extremely intense rockbursts in a water diversion tunnel. Int. J. Rock Mech. Min. Sci. 164, 105359.

Wang, J., Apel, D.B., Wei, C., Xu, H., 2024. Prediction of strainburst risks based on the stiffness theory: development and verification of a new rockburst indicator. Int. J. Rock Mech. Min. Sci. 175, 105667.

Wu, L.X., Li, G.H., Wu, H.P., 2001. Experimental exploration to thermal infrared imaging for detecting the transient process of solid impact. Chinese. Scient. Bulletin. 46 (2), 172–176.

Wu, L.X., Wu, Y.H., Zhong, S., Wang, C.Y., Li, G.H., 2006. Research progresses and directions of detection on rock impaction with thermal infrared imaging. Chin. J. Rock Mech. Eng. 25 (11), 2180–2186.

Wu, H., Settgast, R.R., Fu, P., Morris, J.P., 2021. An enhanced virtual crack closure technique for stress intensity factor calculation along arbitrary crack fronts and the application in hydraulic fracturing simulation. Rock Mech. Rock Eng. 54 (6), 2943–2957.

Wu, Y.Z., He, S.F., Fu, Y.K., Li, J.C., Zhou, P.H., Sun, Z.Y., 2025. Experimental study on the failure evolution of surrounding rock and the response of bolt support under multiple impact loads in mine roadways. Rock Mech. Rock Eng. 1–19.

Xia, Y.M., Rao, S.G., Yang, B.C., 1990. An infrared transient temperature measuring apparatus and its application to the tensile impact testing. J. Exp. Mech. 5 (2), 170–177.

Xiao, D.J., Yang, W.T., Liu, C.J., Hu, R., 2022. Testing of Mode-I fracture toughness of sandstone based on the fracturing mechanism of an explosion stress wave. Rock Mech. Rock Eng. 55 (12), 7731–7745.

Xue, R., Liang, Z., Xu, N., 2021. Rockburst prediction and analysis of activity characteristics within surrounding rock based on microseismic monitoring and numerical simulation. Int. J. Rock Mech. Min. Sci. 142, 104750.

Yang, S.Q., Yang, J., Mu, Z.L., Liu, G.J., Huang, M., Li, K.S., Huang, Y.H., 2024. Experimental study on mechanical behavior, fracture characteristics, and acoustic emission damage characteristics of sandstone under triaxial multistage stress disturbance. Rock Mech. Rock Eng. 57 (10), 8633–8655.

Yue, Q., Wang, Q., Rabczuk, T., Zhou, W., Zhuang, X., Chang, X., 2024. A thermo-mechanical phase-field model for mixed-mode fracture and its application in rock-like materials. Int. J. Rock Mech. Min. Sci. 183, 105907.

Zhang, Z.Z., Gao, F., Liu, Z.J., 2010. Research on rockburst proneness and its microcosmic mechanism of granite considering temperature effect. Chin. J. Rock Mech. Eng. 29 (8), 1591–1602.

Zhang, T., Guo, Z.R., Yuan, F.P., Zhang, H.S., 2018. Investigation on the plastic work-heat conversion coefficient of 7075-T651 aluminum alloy during an impact process based on infrared temperature measurement technology. Acta Mech. Sin. 34 (2), 327–333.

Zhang, K.Y., Liu, B., Lei, Y., Guo, L., Fu, R.D., Zhang, Y.C., Zhang, Y.G., 2023. An iterative algorithm to improve infrared thermographic systems' accuracy in temperature field measurement of aluminum alloys. Measurement 210 (2023), 112547.

Zhang, R., Liu, Y., Zhu, L., Hou, S., Li, Z., Zhao, T., Chen, X., 2024a. Failure characteristics and energy evolution process of delayed and instantaneous basalt rockburst under true triaxial conditions. Int. J. Rock Mech. Min. Sci. 183, 105909.

Zhang, Y., Fang, K., He, M., Liu, D., Wang, J., Guo, Z., 2024b. Rockburst prediction using artificial intelligence techniques: a review. Rock Mech Bull. 3 (3), 100129.

Zhang, D., Zhu, S., Zhou, M., Huang, H., Tong, Y., 2024c. Damage quantification and failure prediction of rock: a novel approach based on energy evolution obtained from infrared radiation and acoustic emission. Int. J. Rock Mech. Min. Sci. 183, 105920.

Zhao, X., Liao, Z., Zhang, X., Cao, P., Li, R., Zhu, J., 2024. Influence of pre-existing crack on rockburst characteristics in coal-rock combination: a laboratory investigation. Int. J. Rock Mech. Min. Sci. 178, 105753.